

Numerical investigation on structural glass beams with GFRP-embedded rods, including effects of pre-stress

Bedon, Chiara; Louter, Christian

DOI

[10.1016/j.compstruct.2017.10.027](https://doi.org/10.1016/j.compstruct.2017.10.027)

Publication date

2018

Document Version

Final published version

Published in

Composite Structures

Citation (APA)

Bedon, C., & Louter, C. (2018). Numerical investigation on structural glass beams with GFRP-embedded rods, including effects of pre-stress. *Composite Structures*, 184, 650-661.
<https://doi.org/10.1016/j.compstruct.2017.10.027>

Important note

To cite this publication, please use the final published version (if applicable).
Please check the document version above.

Copyright

Other than for strictly personal use, it is not permitted to download, forward or distribute the text or part of it, without the consent of the author(s) and/or copyright holder(s), unless the work is under an open content license such as Creative Commons.

Takedown policy

Please contact us and provide details if you believe this document breaches copyrights.
We will remove access to the work immediately and investigate your claim.



Numerical investigation on structural glass beams with GFRP-embedded rods, including effects of pre-stress



Chiara Bedon^{a,*}, Christian Louter^b

^a Department of Engineering and Architecture, University of Trieste, Trieste, Italy

^b Department of Architectural Engineering and Technology, Faculty of Architecture and the Built Environment, Delft University of Technology, The Netherlands

ARTICLE INFO

Keywords:

Structural glass
Glass-Fibre-Reinforced-Polymer (GFRP) composites
GFRP-embedded rods
Pre-stressing force
Experimental tests
Finite Element numerical modelling

ABSTRACT

The bending performance of laminated glass (LG) beams with Glass-Fibre-Reinforced-Polymer (GFRP)-embedded rods is numerically assessed in this paper, based on earlier experimental investigations.

Compared to existing literature efforts related to reinforced glass beams – typically including external steel or FRP tendons and/or reinforcement sections adhesively bonded to glass edges in tension – careful consideration is given to the still rather innovative concept of traditional LG beams that contain pultruded GFRP rods embedded within the interlayer foils. Taking advantage of past experimental results and preliminary Finite Element (FE) outcomes for hybrid glass beams, the quasi-static bending performance at room temperature of several geometrical configurations of LG beams with GFRP-embedded rods is compared. These geometrical configurations include variations in number, size and position of rods. The effects and possible benefits due to initial pre-stressing forces for the GFRP rods are also investigated. As shown for some selected configurations only, GFRP-embedded rods can provide active contribution to traditional LG beams, both in terms of post-cracked resistance and ductility. At the same time, given a reference geometry, a certain level of initial pre-stress can further exploit the potential of the same GFRP rods, acting as pre-tensioned tendons thereby enhancing the initial fracture strength. Several aspects should be properly taken into account to assess and optimize the overall performance of these systems, however, since both their elastic and post-cracked performance are highly sensitive to various mechanical and geometrical input parameters.

1. Introduction and design concept

The application of glass as a structural material in contemporary architecture is ever increasing. However, due to the brittleness of glass, its application as a structural material requires specific attention with respect to its safety performance. To this aim, over the past years, research efforts have focused on a specific safety concept for structural glass beams in which reinforcement tendons are added to the beam configuration.

Structural glass beams are already widely used in design projects for roofs and floors, as well as vertical fins and stiffeners for facades and pavilions.

Generally, in such applications, the reinforcement tendons are adhesively bonded at the tensile zone of the structural glass and are intended to carry the tensile force in the event of glass fracture. As a result, they provide a significant post-fracture load-carrying capacity even when extensive glass fracture occurs (see for example [1–9]). The concept of reinforced glass beam has been investigated for a wide range of reinforcement materials and beam geometries. An extensive

overview is provided in [10]. Other effective solutions include also external pre-stressed tendons [11].

More recently, research efforts are expanding towards post-tensioned glass beams. Rather than adding ‘passive’ reinforcement tendons to a given structural glass beam, the tendons are now activated through a pre-tensioning action, thereby inflicting a beneficial compressive pre-stress on the glass beams. Due to this compressive pre-stress, the initial fracture strength of the annealed glass beam – which is governed by its limited tensile strength – is enhanced, while the post-tensioning tendons still guarantee a significant post-fracture load-carrying reserve (see for example [12–14]). An overview of recent research activities in the field of post-tensioned glass beams is included in [10], while comparative Finite-Element (FE) numerical investigations on glass beams with unbonded steel or adhesively bonded, post-tensioned steel or CFRP tendons are presented in [15], [16] and [17] respectively.

The current paper adds to the investigations into reinforced and post-tensioned glass beams. Compared to most of related existing studies, however, instead of adding reinforcement tendons at the outer perimeter of a given structural glass beam sections, the actual research

* Corresponding author at: Department of Engineering and Architecture, University of Trieste, Piazzale Europa 1, 34127 Trieste, Italy.
E-mail address: chiara.bedon@dia.units.it (C. Bedon).

investigation aims to integrate reinforcement tendons within the web of the beams. This goal is achieved by embedding Glass-Fibre-Reinforced-Polymer (GFRP) tendons in the interlayer of glass sections. More specifically, small pultruded GFRP rods are intended to be laminated by means of polymer interlayers between the individual glass plies of a given laminated glass (LG) unit, using a regular autoclave lamination process. The GFRP rods act as reinforcement tendons and all their interaction with the adjacent glass panels is provided through the polymer interlayer foils. GFRP is selected because of its high tensile strength which is, despite its brittle response, expected to enhance the post-fracture strength of structural glass beams as compared to more common reinforcement materials for glass beams such as stainless steel or timber. Additionally, GFRP has a translucent appearance, thereby minimizing the visual impact on the glass beam as opposed to other opaque reinforcement materials.

The structural validity of the explored design concept has already been demonstrated experimentally in [18]. There, through four-point bending experiments carried out on 1.5 m long, LG beams with embedded GFRP rods, it was shown that such beams are able to reach significant post-fracture loads, well beyond the initial fracture load. However, apart from those past experiments, the design concept has to date not been further explored. The current paper, in this context, takes the existing bending experiments as a basis for a more extended FE parametric study, aiming to investigate more in detail the actual structural performance of the examined structural typology. In doing so, careful consideration is given in ABAQUS [19] to a series of geometrical aspects, including size, number and position of rods. In addition, the paper investigates the structural effects deriving from possible pre-tensioning of the same embedded GFRP rods, such as done in the post-tensioned glass beam concept, thereby targeting for an enhanced initial fracture strength and an improved post-fractures performance. As shown, however, the overall performance depends on a multitude of aspects, which should be properly combined in order to maximize the benefits of the explored design concept.

2. Summary of past experimental tests

The full FE investigation proposed in this paper is carried out on the basis of past experimental studies presented in [18].

There, all the beam specimens, with a nominal length of 1.5 m, consisted of a double-layer LG section, with 8 mm × 115 mm the size of each glass panel and a bonding SentryGlas® (SG) interlayer [20]. Two different beam typologies were tested, by changing the type, number and size of pultruded GFRP rods, including beam specimens with 3 flat embedded rods (S-glass filaments within an epoxy matrix resin), as well as 5 round rods (E-glass filaments within a polyester matrix), both embedded in a SentryGlas® (SG) interlayer and positioned in accordance with Fig. 1(a) and (b).

Within the typical beam specimen, the SG foil was composed of 3 sheets, for a total nominal thickness up to ≈ 3.9 mm (1.52 mm for external layers, plus 0.8 mm for the middle one) and ≈ 4.5 mm (1.52 mm × 3) for beam specimens with flat or round rods respectively. During the assembly stage, the middle SG sheet was properly cut, to host the GFRP rods, so that the same rods could be kept in their correct position during the lamination process.

For both beam types, 2 specimens were tested in accordance with the test setup provided in Fig. 1(c). All the experiments were carried out under laboratory conditions, with 23 °C the average temperature. The specimens were loaded until first cracking by imposing a displacement rate of 1 mm/min. For the post-cracked stage only, the imposed deflection rate was increased stepwise to 2 and 5 mm/min, up to collapse of the specimens. In doing so, the applied vertical load and the corresponding mid-span deflection were continuously monitored.

In Table 1, additional geometrical and mechanical properties are given for the flat or round GFRP rod types, in accordance with [18,20,21]. Based on the nominal cross-section of glass given in

Fig. 1(a) and (b), moreover, for comparative purposes Table 1 also reports the calculated non-dimensional R_A values for both the beam types, being representative of the ratio between the total cross-sectional area of glass ($A_{glass} = 2 \times 8 \times 115 = 1840 \text{ mm}^2$) and the total cross-sectional surface $A_{rod,tot}$ of rods (i.e. A_{rod} multiplied by the number of rods n_{rod}).

3. Finite Element numerical study

3.1. Assembly, mesh and interactions

Based on Section 2, the full FE investigation was carried out in this research study on several geometrical configurations of LG beams reinforced with GFRP-embedded rods. Beside the specific geometrical features of the two typologies of beam specimens described in Fig. 1(a) and (b), the same general FE assumptions were taken into account when describing, assembling and calibrating the so called ‘MF-n3’ (‘M’ = model, ‘F’ = flat rods, with $n_{rod} = 3$) and ‘MR-n5’ (round rods, $n_{rod} = 5$) models.

Basically, due to symmetry, half specimen only was described in these FE models, by taking into account the longitudinal plane of symmetry of the examined specimens (see Fig. 2). Aiming to ensure the computational efficiency and accuracy of numerical simulations, optimized FE models were developed. In them, a combination of 3-node and 4-node monolithic *shell* elements (S3R and S4R type of ABAQUS library [19]) was in fact used for the description of each glass panel. 8-node *solid* brick elements were taken into account for the SG foils only (C3D8R type [19]), so that they could physically host the GFRP tendons. For the latter components, beam elements (B31 type [19]) were finally used, with nominal cross-sectional properties provided in Table 1, and positioned in accordance with Fig. 1(a) and (b).

Mesh pattern and size was chosen so that reliable predictions on crack propagation in glass could be obtained, for the examined loading configuration. As such, the reference size of mesh elements was refined in the beam region subjected to tensile stresses (with 2 mm the average edge length of shell and solid elements), but increased up to a maximum of 15 mm for the beam region mainly subjected to compression stresses due to bending. The final assembly hence consisted of a set of 6000 elements and 33,000 degrees of freedom.

A key role was then assigned to mechanical constraints, in order to ensure an appropriate structural interaction between all the FE model components. At the glass-to-SG interface, a surface distributed “*tie*” constraint was used, so to avoid possible relative displacements and rotations between all the interested mesh nodes [19]. The “*embedded*” constraint option was then defined for each one of the GFRP rods, so that they could be physically hosted by the surrounding SG layer [19].

Due to symmetry of the FE model, appropriate boundary conditions were finally considered, along the mid symmetry axis of the beam, as well as to account for the bending test protocol of the specimens.

3.2. Materials

The mechanical characterization of materials models was based on past literature projects (see for example [15–17]) and technical data-sheets (i.e. [21,22]). Constitutive laws and damage models for glass, SG and GFRP, in particular, were selected to optimize the accuracy of FE predictions for the bending performance of the examined beam typologies, under monotonic static loading and ambient temperature.

In the case of float annealed glass, the *concrete damaged plasticity* (“CDP”) material model was used [19]. In accordance with material product standards [23], the nominal characteristic tensile strength $\sigma_{tk} = 45 \text{ MPa}$ was taken into account, with reference nominal values also for modulus of elasticity ($E_{glass} = 70 \text{ GPa}$) and Poisson ratio ($\nu_{glass} = 0.23$). In terms of compressive resistance, a conventional value $\sigma_{ck} = 1000 \text{ MPa}$ [23,24] was indeed considered, as also in accordance with the numerical investigation proposed in [15].

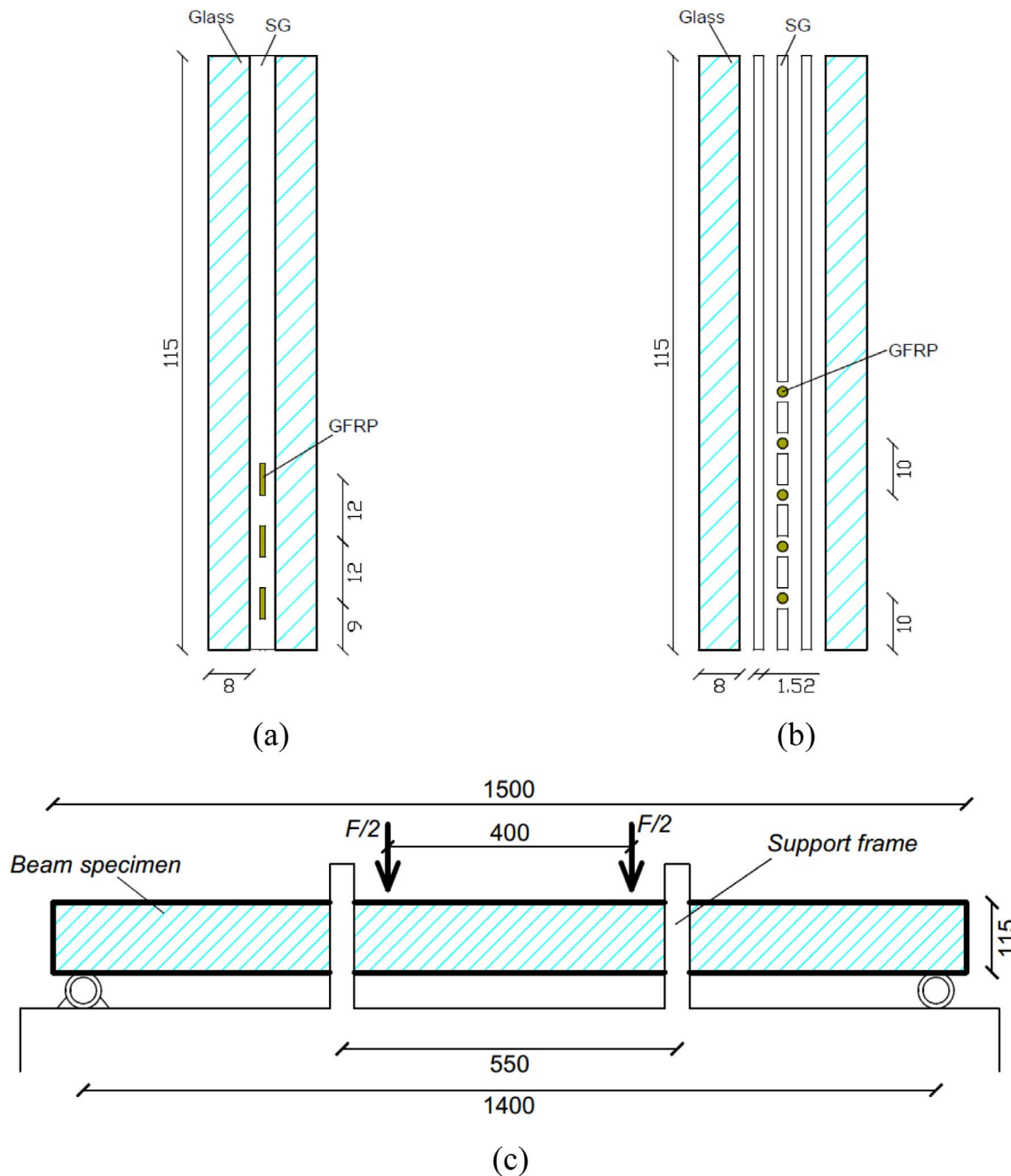


Fig. 1. Reference cross-section (exploded and assembled) for the beams experimentally investigated in [18], with evidence of geometrical features of specimens with (a) flat and (b) round GFRP-embedded rods, and (c) test setup (front view). Nominal dimensions given in mm.

The CDP damage model (see the ABAQUS Theory Manual for an extended theoretical background [19]), describes the inelastic compressive and tensile behaviours of a given brittle material in the form of a multi-hardening plasticity and a scalar isotropic damaged elasticity characteristic curves (see Fig. 3). In this research study, the main post-cracked input parameters were defined in accordance with earlier research contributions as well as literature references (see also [15] for the CDP calibration considered in the current study), so to account for the brittle behaviour of glass. In doing so, to avoid additional numerical instabilities for the post-cracked stage predictions, the physical deletion of cracked shell elements from the mesh pattern was then fully disregarded. As such, failed glass elements with almost null residual stiffness and strength were not removed from the 3D assembly. In terms of post-processing of the obtained FE data, a direct effect of this modelling assumption was the lack of visual cracks in glass shell elements.

The first occurrence of tensile damage as well as the propagation of cracks in the LG beam up to collapse, consequently, was in any case continuously monitored in the form of damage energy evolution and distribution of stresses in the glass elements.

For SentryGlas®, based on the purpose of the current FE investigations, an equivalent, linear elastic mechanical behaviour was taken into account. Possible viscoelastic effects, in this sense were fully neglected on the overall performance of the examined specimens. The equivalent elastic stiffness of SG foils ($E_{SG} = 120$ MPa) was calibrated on the base of the average duration of the experiments (≈ 30 – 45 min) and past literature projects (see for example [6,25,26]).

In the case of GFRP rods, their brittle elastic constitutive behaviour in tension was reproduced by means of an equivalent elasto-plastic stress-strain relationship. A tensile damage criterion was also properly calibrated, via the ‘ductile damage’ material option available in

Table 1
Geometrical and mechanical properties of GFRP rods, depending on the beam type [18,21,22].

		Flat rods	Round rods
Rod size	[mm]	0.8 × 6	φ 2 (diameter)
Rod area	[mm ²]	A_{rod}	3.1
Number of rods	–	n_{rod}	3
Total area	[mm ²]	$A_{rod,tot}$	23.04
Glass-to-GFRP ratio	–	R_A	≈ 130
Volume fraction	[%]	v_{rod}	60–65
Glass fibre filaments type	–	–	S-glass
Tensile strength (virgin nominal)	[MPa]	$\sigma_{rod,v}$	4600
Tensile strength (nominal)	[MPa]	σ_{rod}	2760–2990
Modulus of elasticity	[MPa]	E_{rod}	83000–90000
			73000

ABAQUS, so that the single rod in bending could manifest a fully brittle collapse mechanism when first achieving the ultimate tensile resistance/strain. To this aim, the elastic modulus, ultimate resistance and failure strain were derived from technical data-sheets of the producer (see Table 1).

3.3. Loading

Displacement-controlled simulations were carried out in ABAQUS/Explicit [19], in the form of dynamic analyses with quasi-static increase of imposed vertical displacements.

Based on the assumed mechanical models for materials, as well as on the test setup provided in Fig. 1(c), the assigned bending deflections were gradually increased on both the reference FE models representative of experimental specimens with flat or round rods. Accordingly, the evolution of reaction forces, mid-span deflection, as well as stress distribution and damage initiation and propagation in the various beam components was continuously monitored. In doing so, the maximum imposed displacement was set up to 100mm, being representative of ≈ 1/15 the total span. The ultimate failure configuration for each beam – being dependent on possible collapse mechanisms occurring in glass (i.e. tensile cracking and/or crushing phenomena), in

the GFRP rods (tensile brittle failure) or in the SG foils (yielding and tearing) – was hence predicted for them.

3.4. Preliminary FE analyses and discussion of results

The so assembled MF-n3 and MF-n5 models were first used to run preliminary numerical analyses on the reference experimental beams, so to compare the numerical predictions with full-scale bending test results derived from [18].

The so obtained data are collected in Table 2 – in the form of key values for measured loads and displacements – as well as in Fig. 4 for the full load vs. mid-span deflection response. Basically, as also experimentally observed at the time of the past research project [18], the examined beam typology proved to offer well promising structural performances, compared to the same geometry with a traditional LG section only. The latter aspect is also emphasized in Table 2, where the first cracking configuration (i.e. (F_I, u_I) values) and the ultimate, post-cracked performance parameters (i.e. (F_{max}, u_{ult}) values) are compared for the past experimental test specimens, the corresponding FE models (MF-n3, MR-n5), as well as a further FE model representative of the same beam geometry and loading setup, but deprived of the GFRP rods (i.e. ‘no rods’ columns in Table 2). There, F_{max} denotes the post-fracture peak value sustained by the beams, while u_{ult} represents the ultimate mid-span deflection at collapse.

As far as the full load-displacement response of the same beams is also considered for comparative purposes, in place of selected load/deflection values collected in Table 2, it is possible to perceive a rather close correlation between the proposed FE models and the corresponding test measurements, see Fig. 4.

For both beam types, in particular, the actual bending response is namely characterized by three specific phases, including (i) the elastic stage, (ii) the first cracking phase and (iii) collapse. Initially (i), the elastic stiffness is predominantly given by the glass panes, due to negligible in-plane flexural contribution of SG foils as well as limited stiffness of GFRP rods, compared to glass. For the same reason, it can be noticed from Table 2 that the ‘no rods’ FE model is mainly characterized by a linear elastic response, in which first cracking mostly coincides with GFRP-reinforced specimens.

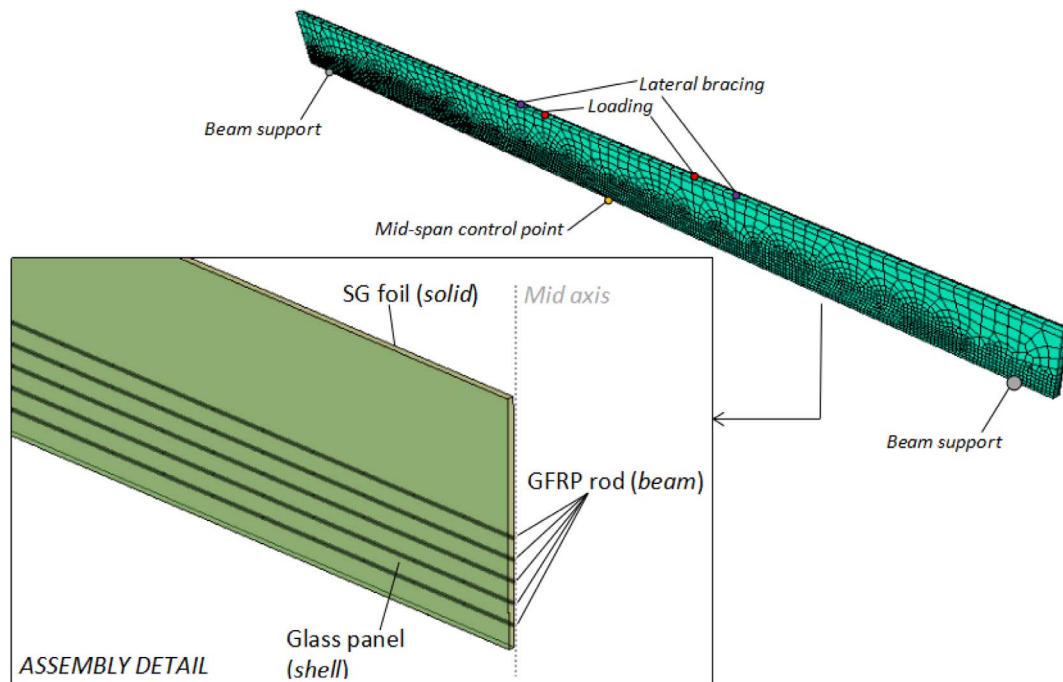


Fig. 2. Overview of the typical FE model representative of half beam specimen, with assembly detail (mesh pattern hidden) referred to beams with round rods (MR-n5, ABAQUS [19]).

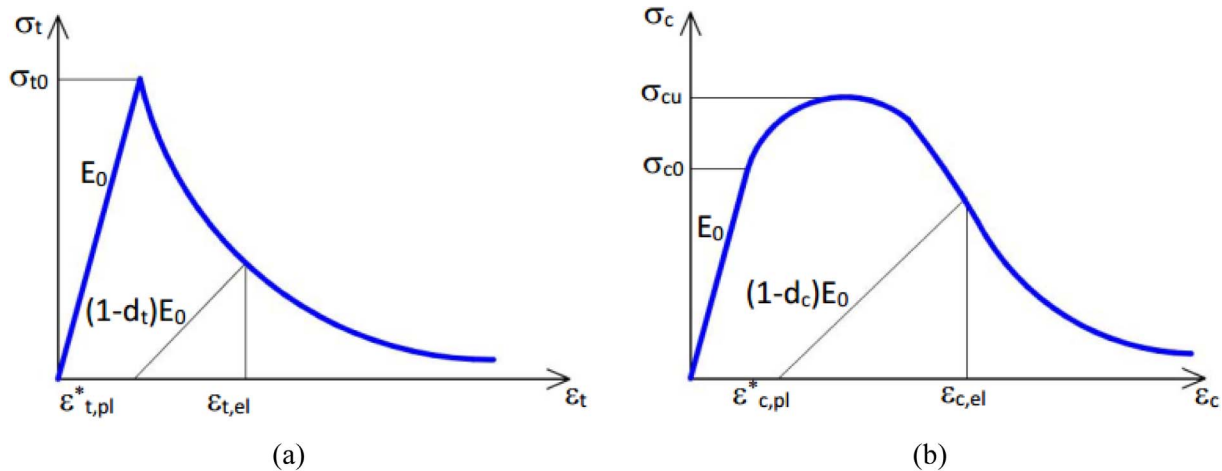


Fig. 3. Mechanical constitutive laws for the CDP model representative of (a) tension and (b) compression behaviours (ABAQUS [19]). Input parameters derived from [15].

Table 2

Experimental results for specimens with flat and round rods, in accordance with [18], and corresponding FE predictions (ABAQUS [19]). $R_F = 100 \times F_{max}/F_1$, $R_u = 100 \times u_{ult}/u_1$, $\Delta_{FE} = 100 \times (v_{FE} - v_{TEST})/v_{TEST}$.

	Flat rods (F-n3)						Round rods (R-n5)						No rods	
	F_1 [kN]	u_1 [mm]	F_{max} [kN]	u_{ult} [mm]	R_F [%]	R_u [%]	F_1 [kN]	u_1 [mm]	F_{max} [kN]	u_{ult} [mm]	R_F [%]	R_u [%]	F_1 [kN]	u_1 [mm]
EXP Avg.	5.5	2.9	11.6	81.5	210	2810	6.8	3.3	7.8	51.6	115	1563	–	–
St. Dev.	0.5	0.5	0.5	4.2	–	–	1.5	0.8	0.1	3.9	–	–	–	–
FE	5.7	2.3	12.9	77.8	226	3382	6.5	2.3	9.1	60.6	140	2634	5.6	2.3
Δ_{FE} [%]	3.6	–20.6	11.2	–4.5	–	–	4.4	–30.3	16.6	17.4	–	–	–	–

The major effect of GFRP-embedded rods, in this regard, lies in the marked benefit the LG beams can achieve, in terms of residual resistance and maximum deformations in the post-cracked stage, hence resulting in a marked improvement of redundancy and ductility, compared to traditional LG beams.

Actually, from the numerical and experimental data collected in Table 2 and Fig. 4, it is possible to notice that FE models tend to overestimate the elastic stiffness of specimens (≈ 1.89 kN/mm and ≈ 2.06 kN/mm the average test value for beam specimens with flat and round rods respectively), up to $\approx 30\%$ the experimental value for both beams typologies. This scatter, as also in accordance with earlier comparative applications for structural glass beams (see for example [15–17]) can be explained by possible local deformations of the experimental setup, being the latter values actually included in the measured vertical deflection of the specimens control point but not accounted by the corresponding FE models.

In terms of first cracking load F_1 , in addition, it can be seen from Table 2 and Fig. 4 that for the specimens with flat rods but especially in the case of the specimens with round rods, the assumption of a nominal value for the tensile resistance of glass generally provides close correlation with experimental average values of first fracture loads for both beam typologies. In any case, the high scatter in the actual glass strength (up to 30% the usual range of variation from nominal values, see also [27]) can lead also to partial discrepancy between test results and corresponding FE predictions. This is the case of round rod specimens, where marked variations were observed in terms of first cracking load for the two specimens (see especially the ‘EXP R-n5-#2’ plot in Fig. 4(b)), as well as for the corresponding FE model.

In any case, rather interesting correlation was generally noticed between FE simulations and reference test results, in terms of global bending performance up to collapse of the specimens. Collapse mechanism, in particular, was typically associated to wide propagation of tensile cracks in glass, with progressive decrease of the post-cracked stiffness for both the beam typologies (see also [18]). Cracks opening

and propagation can be also perceived in Fig. 4 in the form of progressive drops for the measured load-deflection curves, with rather appreciable correspondence between experimental and FE data. Through stage (ii) of the simulation process, the actual post-cracked resistance mainly depends on the residual glass section, but takes advantage from the GFRP rods acting as tensile tendons for the damaged beams. As a consequence, the specimens are able to sustain additional loads as far as the GFRP rods themselves lie in the elastic range. Also in this case, from Fig. 4(a) and (b), it is possible to notice – beside the lack of additional small scale tests on single components, to further calibrate the input material properties – that both the MF-n3 and MR-n5 FE models including nominal tensile resistance of GFRP rods proved to estimate with rather interesting accuracy the ultimate configuration of the corresponding experimental specimens, hence suggesting a further extension of the same FE numerical study, aiming to investigate more in detail the potential and actual performance of the examined structural typology.

4. Extended FE parametric study and discussion

Based on FE methods and preliminary outcomes presented in Section 3, a further extended parametric investigation was carried out on the same beam typology, so that major effects of some input parameters (i.e. number and position of GFRP rods, for a given glass beam geometry) could be analysed.

At a following stage of the parametric study, see Section 4.2, the benefits of possible pre-stressing forces for the GFRP rods were also investigated, in order to further optimize the overall structural performance of such beams.

4.1. Effect of GFRP rods number, section, position

Given the MF-n3 and MR-n5 geometrical properties summarized in Fig. 1 and Table 1, as well as the FE methodology described in Section

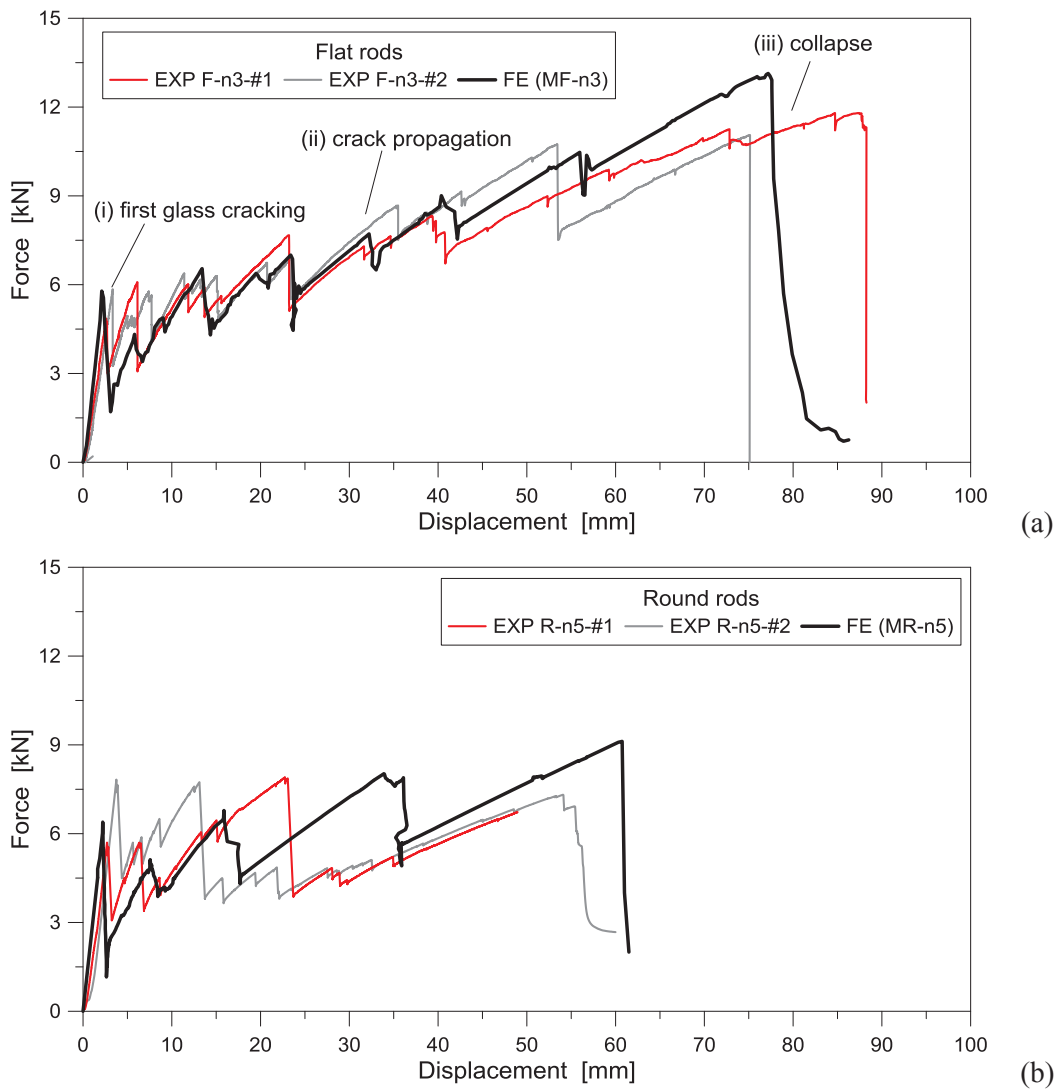


Fig. 4. Experimental [18] and numerical (ABAQUS [19]) load-displacement response of beam specimens with (a) flat or (b) round GFRP rods, in accordance with Fig. 1.

Table 3
Geometrical properties of selected FE models for parametric analyses on LG beams with GFRP rods.

	Reference models		Round rods			Bottom tendon
	MF-n3	MR-n5	MR-n3	MR-n7	MR-n10	M-Bot
A_{rod}	mm ²	4.8	3.1	3.1	3.1	15.5
n_{rod}	-	3	5	3	7	10
$A_{rod,tot}$	mm ²	23.1	15.5	9.3	21.7	31
R_A	-	130	120	200	85	60

3, additional configurations were numerically investigated for the same glass beams. Basically, the total number n_{rod} and/or the total section $A_{rod,tot}$ of GFRP rods – hence their position along the section height – was first modified, compared to the MF-n3 and MR-n5 systems. Selected cases are summarized in Table 3 and Fig. 5, with evidence of corresponding pattern for the GFRP rods.

For comparative purposes only, a further reinforcement configuration was also considered, as labeled in Table 3 and Fig. 5 by ‘M-Bot’ model (‘Bot’ = bottom tendon). In the latter case, in particular, the same total section $A_{rod,tot}$ of the MR-n5 test specimen was used (i.e. $R_A = 120$), but the GFRP reinforcement was assumed to consist of a single tendon only, with full solid cross-section, and to lie along the

tensile edge of the glass beam (see Table 3 and Fig. 5).

As shown in Fig. 6(a), given their almost comparable amount of GFRP rods (i.e. R_A coefficient for the MF-n3 and MR-n5 reference beams), no marked variations were noticed in the overall bending performance of the corresponding FE models, despite the different number of rods ($n_{rods} = 3$ and 5 for them, respectively). Rather close correlation between the MF-n3 and MR-n5 plots can be noticed also in terms of post-cracked stiffness, being this latter parameter mainly dependent on the bending stiffness of GFRP rods rather than on the residual (almost negligible) contribution of severely cracked glass panels.

As a result, further parametric investigations were mainly focused on the effects due to variation in the total amount $A_{rod,tot}$ of GFRP rods on the actual bending performance of the examined glass beams, as also in accordance with Table 3.

Globally, a rather stable flexural performance was observed by changing n_{rod} .

Fig. 6(b) compares the bending performance of the MR-n3, MR-n5 and MR-n10 cases, being the intermediate MR-n7 curve omitted for clarity of presentation, with evidence of the first 30mm of measured mid-span deflection. As shown, due to the examined bending loading configuration, the increase of GFRP-embedded rods number for the reference MR-n5 specimen does not modify the overall flexural response of the analysed beams (i.e. plots give for MR-n7 and MR-n10 beams). Partial post-cracked stiffness and resistance decrease can be

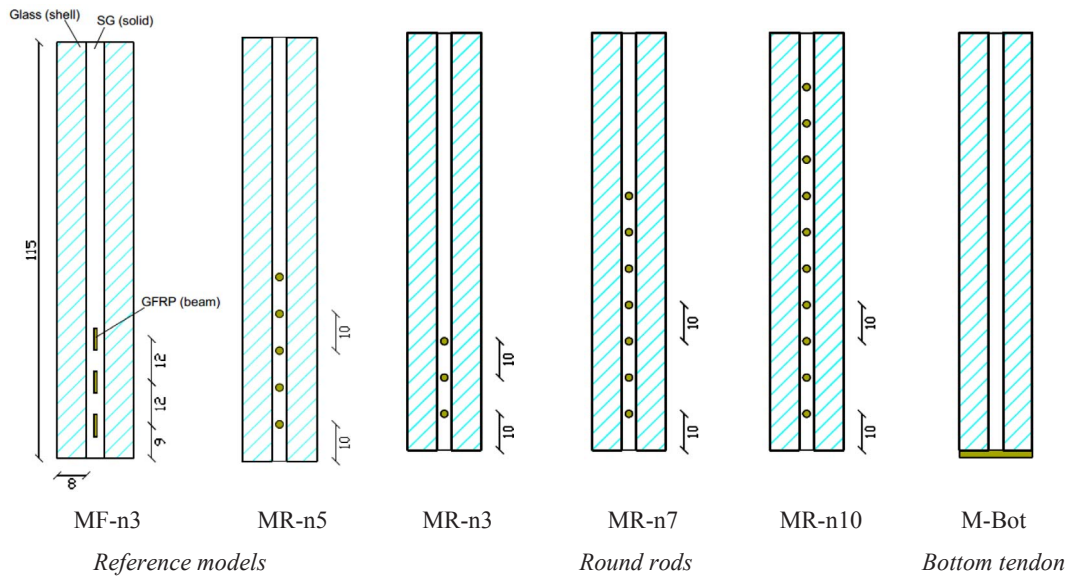


Fig. 5. Schematic cross-section of beams with different number and/or amount of GFRP rods, in accordance with Table 3 (nominal dimensions given in mm).

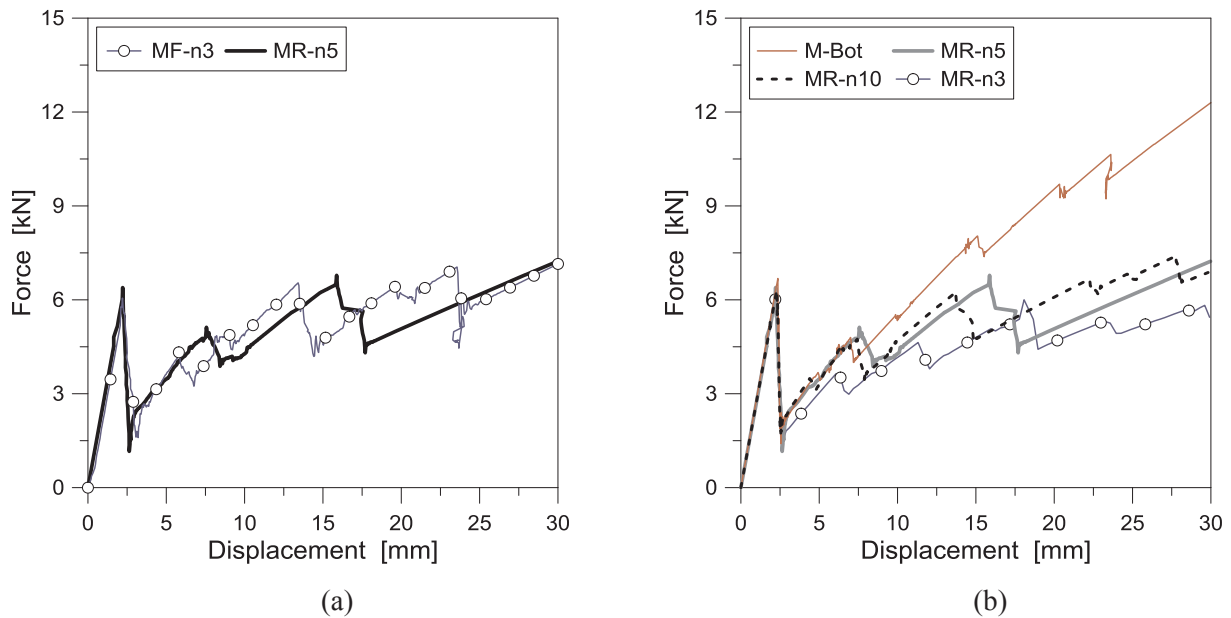


Fig. 6. Numerical load-displacement response (ABAQUS [19]) of beam specimens with different geometrical configurations and/or total amount for the GFRP rods, in accordance with Table 3.

noticed for the MR-n3 beam only ($R_A = 200$), compared to the MR-n5 model. In any case, for all of the MR-n3, MR-n5, MR-n7 and MR-n10 beams, first cracks was observed to occur at ≈ 2.3 mm of deflection, with ≈ 6.5 kN the corresponding load fracture load. After 30 mm of mid-span deflection, the glass panes were noticed to be mostly fractured, even with all the GFRP rods still in the elastic range, with maximum stresses in the order of ≈ 1450 MPa for the bottom rods only subjected to maximum bending effects. Worth of interest in Fig. 6(b) is the post-cracked contribution of rods for the MR-n3 beam, where – even in presence of a limited amount of GFRP total section for tendons (i.e. $R_A = 200$) – the GFRP embedded reinforcement can still offer a rather stable behaviour to the almost cracked glass panels.

In this regard, Fig. 7(a)-to-(d) present a typical (qualitative) propagation of cracks in glass, with evidence of tensile distributions at different mid-span deflections (5, 10, 20 and 30 mm), as observed for the reference MR-n5 model. There, cracks in glass can be perceived to locate and propagate thanks to concentration and distribution of

stresses.

The performed FE simulations highlighted, for example, that additional GFRP rods in the top region of the beam (i.e. MR-n7 or MR-n10) would not provide any kind of global structural effort for the cracked glass panes, compared to the reference MR-n5 configuration, neither in terms of post-cracked stiffness (as also highlighted in Fig. 6(b)) nor in terms of crack propagation (i.e. Fig. 7(a)-to-(d)). However, major benefits can be expected for the explored beam configurations especially under cyclic loading conditions, hence suggesting the suitability and feasibility of an optimized FRP-embedded rod reinforcement, as well as the need of further investigations inclusive of various loading conditions.

A rather different performance was indeed observed for the M-Bot system, in which some benefits due to the application of a bottom full solid GFRP section at the tensile edge of glass panes can maximize the bending performance of the examined beams, for the investigated loading condition. While the first cracking load is mostly comparable to

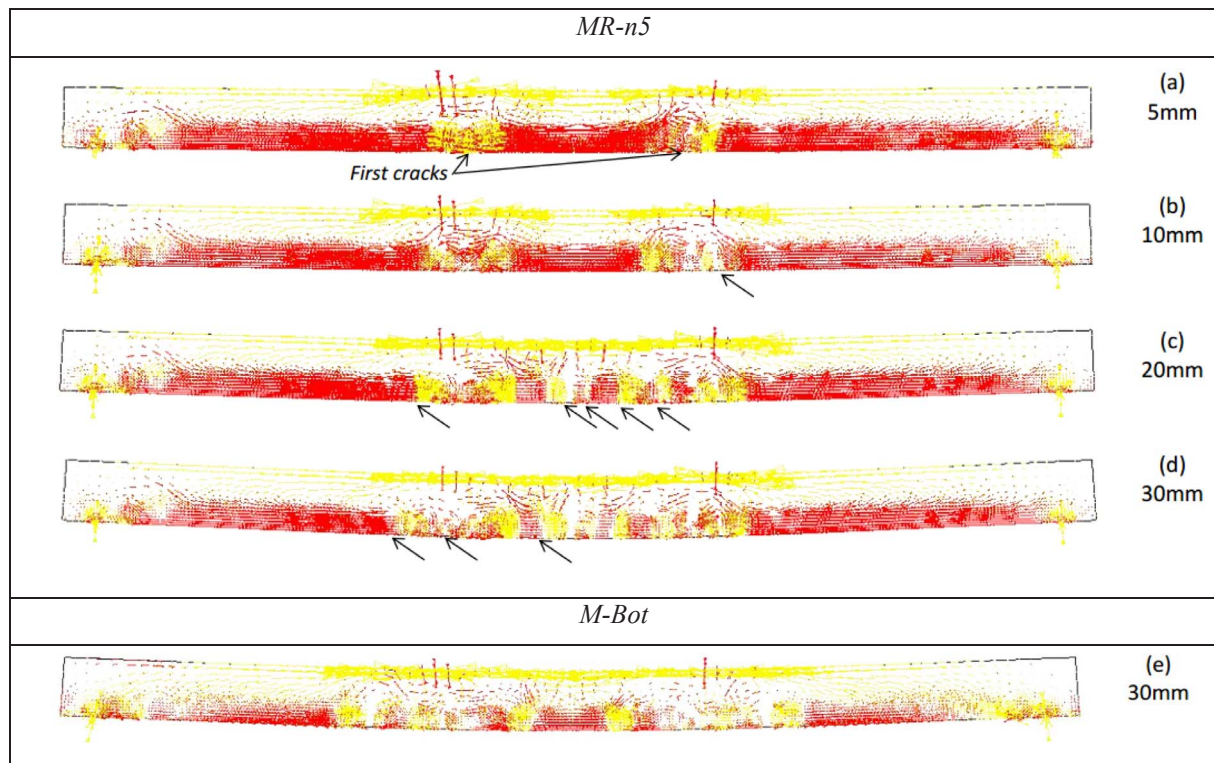


Fig. 7. Numerical distribution of principal stresses in glass, for different mid-span deflections (vectorial representation, front view). Results collected for (a)-(d) MR-n5 beam or (e) M-Bot beam (ABAQUS [19]). Arrows indicate crack initiation points.

the MR-n5 solution as well as the other beams with GFRP-embedded rods in general, from Fig. 6(b) it is in fact possible to perceive that maximum efforts due to the bottom tensile tendon can be achieved in terms of post-cracked stiffness for the fractured assembly, due to more favorable position of the tensile GFRP tendon. However, see Fig. 7(e), given a reference deflection of 30 mm, qualitatively larger cracks can be also observed in the glass panes of the M-Bot system, compared to beams with GFRP-embedded rods (i.e. Fig. 7(d)), hence giving further evidence of the key performance aspects and difference between the two beam typologies.

4.2. Effect of pre-tensioned GFRP rods

4.2.1. General modelling assumptions

At a second stage of the FE parametric study, the effects and potential benefits of additional pre-stressing forces in GFRP rods were investigated. In doing so, some of the geometrical configurations discussed in Section 3.1 and Table 3 were further analysed, including the effects of various levels for the initial force P_0 imposed in the rods. In accordance with Section 3.1 and Fig. 1(c), in addition, the same boundary conditions and symmetry assumptions were accounted for the examined beams, through the FE modelling phase. The actual result of lateral bracings in accordance with the experimental setup, for example, is the prevention of possible lateral-torsional buckling phenomena in such beams, hence the latter issue should be separately assessed and properly prevented. While standardized design methods are in fact available in the literature for simple glass structural elements under various loading and boundary conditions (i.e. [28]), the actual lateral-torsional buckling response and resistance of similar hybrid beams should be properly assessed, including the effects due to continuous lateral supports and interacting structural elements as a part of full assemblies they belong [29–31].

As also shown in [16,17], as well as in agreement with the mechanical performance of reinforced concrete members, as far as an optimal level of pre-stress is imposed to tendons for a given beam

geometry, important benefits can be achieved in its overall structural performance. This is true especially in the case of glass and hybrid glass systems, due to the intrinsic tensile brittleness of material, as well as to the mostly limited thickness of glass panes composing a LG section.

As a general rule for the FE study inclusive of pre-stressing effects, compared to Section 3, few key variations were preliminary implemented in the typical FE numerical model, so that the pre-stressing stage and its effects on the fully composite assembly could be properly described and taken into account, in the form of an initial stress state for the subsequent bending analysis.

The typical simulation consisted in fact, as also in accordance with [16,17] and Fig. 8, in a combination of three subsequent steps carried out both in ABAQUS/Standard and ABAQUS/Explicit [19], and namely represented by (I) pre-stressing of the GFRP rods alone; (II) release of the GFRP rods + adhesive bonding phase; (III) bending test on the composite beam. First, step (I), the post-tensioning phase was numerically reproduced in the form of a static incremental analysis. At this stage, the average experimental value of the imposed pre-stressing force P_0 was assigned to the steel tendon only, by means of an imposed equivalent initial stress σ_{p0} .

Given an initial force value P_0 for the single rod with A_{rod} cross-section, in particular, the non-dimensional parameter R_{p0} parameter was defined as:

$$R_{p0} = \frac{\sigma_{p0}}{\sigma_{rod}} = \frac{P_0}{A_{rod} \sigma_{rod}} \quad (1)$$

with A_{rod} and σ_{rod} given in Tables 1 and 3.

During step (I), no mechanical interaction was considered between the GFRP rods and the glass beam. Once attained the desired level of initial pre-stress in the GFRP rods alone, the release & laminating stage was reproduced in the form of a second static incremental step (phase (II)). At this stage, the ‘embedded’ constraint early described was imposed at the interface between the GFRP rods and the SG layer, so that the middle interlayer could physically host the tendons. In addition, further rigid restraints (nodal tie option) were imposed between each

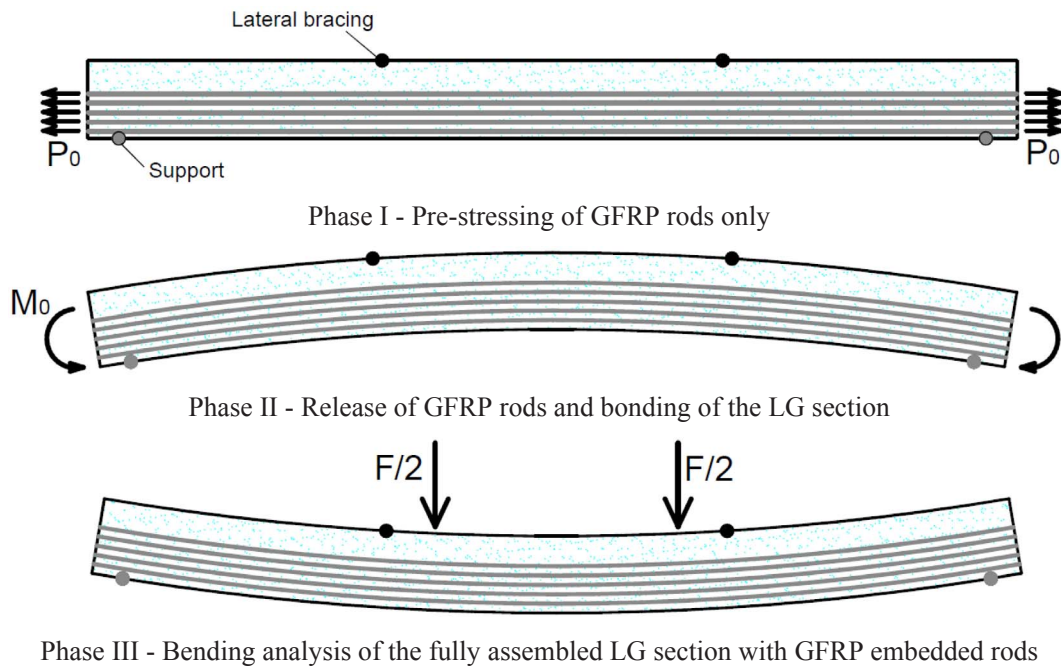


Fig. 8. Schematic representation of FE modelling approach for GFRP-reinforced glass beams with initial pre-stress.

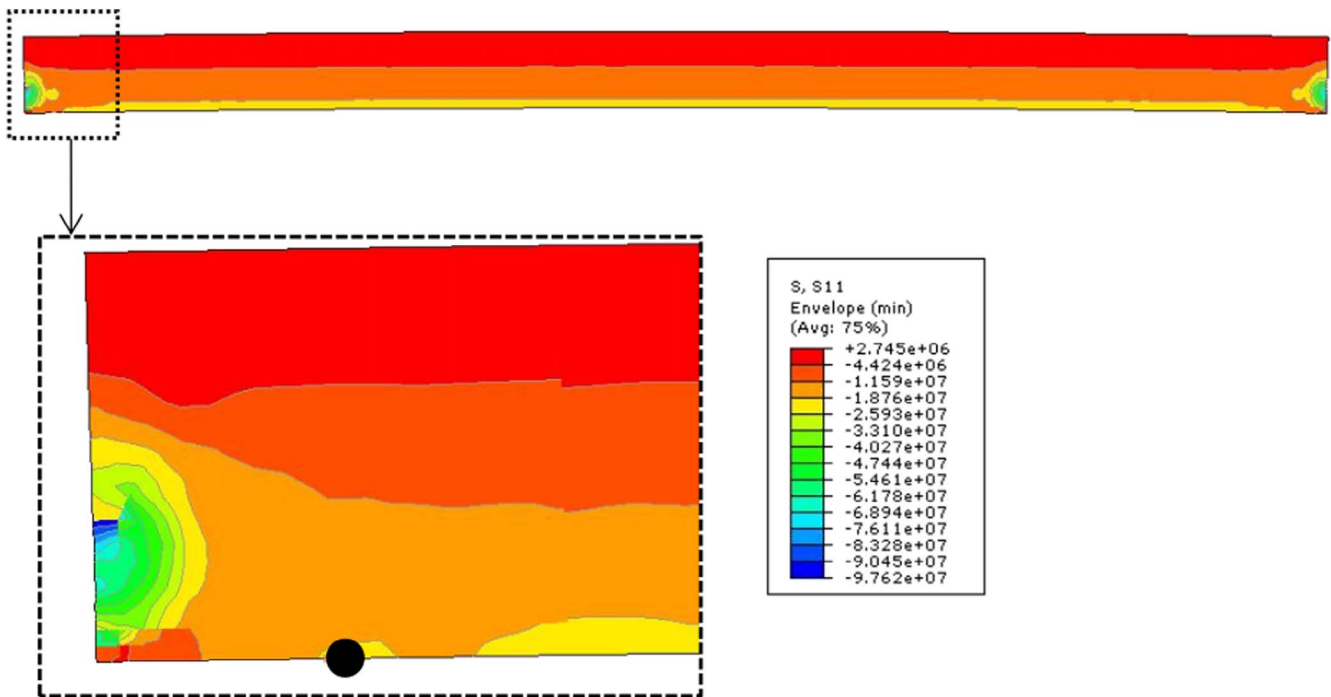


Fig. 9. Typical effects of initial pre-stressing forces in terms of stress distribution in the glass panes, overall view with detail close to the beam ends (ABAQUS [19]). Example referred to the MR-n5 beam, with $R_{p0} = 0.50$ (front view, with stress values given in Pa).

GFRP rods end and the adjacent glass edges, so to account – after the release of pre-stressed rods – the presence of small metal gaskets able to keep rods themselves in their position, hence to provide a certain (even local) structural interaction between GFRP rods and glass panels. The primary aim and consequence of these latter FE assumptions is in fact that the GFRP rods, once released, could exhibit their beneficial effects in the form of an imposed upward bending for the glass beam (M_0 , in Fig. 8), with a corresponding bi-triangular distribution of initial stresses in the glass layers. Due to fixed end restraints for the GFRP rods, such a kind of effect is ensured also in presence of relatively weak interlayers. On the other hand, the occurrence of additional stress peaks in the glass

(i.e. Fig. 9 and related comments) should be properly checked.

Finally (phase (III)), the four-point bending test simulation was carried out on the so assembled GFRP reinforced composite system (see also Section 3).

As a key aspect of performed FE simulation, careful consideration was paid for the evolution of maximum stresses in all the assembly components, during the full simulations and phases I-to-III. As far as the GFRP rods subjected to an initial pre-stressing force P_0 and then released are expected to mainly manifest in the form of an upward bending deformation for the examined full composite beams, further peaks of stresses are also expected close to the end edges of glass panes,

Table 4

FE parametric analysis of glass beams with GFRP-embedded rods, including pre-stressing force. $R_F = 100 \times F_{max}/F_1$, $R_u = 100 \times u_{ult}/u_1$. (*) stress values referred to mid-span section.

FE Model	Pre-stress effects only (*)				Bending performance					
	R_{p0} Eq. (1)	u_{0+} [mm]	$\sigma_{c,0}$ [MPa]	$\sigma_{t,0}$ [MPa]	F_1 [kN]	u_1 [mm]	F_{max} [kN]	u_{ult} [mm]	R_F [%]	R_u [%]
MR-n3	–	0	0	0	6.5	2.3	7.7	55.7	118	2422
	0.25	0.29	–7.08	1.87	7.2	2.6	8.4	48.7	117	1873
	0.5	0.58	–14.16	3.78	8.4	3.1	8.1	17.8	96	574
	0.75	0.88	–21.25	5.59	9.7	3.6	7.8	15.2	81	157
MR-n5	–	0	0	0	6.5	2.3	9.1	60.6	140	2634
	0.25	0.36	–9.88	1.34	7.6	2.8	11.9	58.7	157	2097
	0.5	0.73	–19.76	2.64	9.3	3.5	11.4	40.5	122	1157
	0.75	1.09	–29.64	4.11	10.5	3.8	11.4	13.4	109	352
MR-n10	–	0	0	0	6.5	2.3	9.1	60.9	140	2636
	0.25	0.07	–9.21	–7.28	7.7	2.8	12.1	58.8	157	2100
	0.5	0.14	–18.60	–14.57	8.9	3.2	12.9	38.6	144	1206
	0.75	0.21	–27.89	–21.86	10.2	3.7	13.9	26.8	136	724

i.e. where the GFRP rods are restrained and local effects can occur.

In this regard, Fig. 9 gives evidence of the typical distribution of stresses in glass at the end of phase II. There, the initial stresses due to P_0 are proposed for the MR-n5 beam, with $R_{p0} = 0.5$. As far as the geometry and configuration of GFRP rods modifies and the imposed P_0 also changes in magnitude, it is clear that crushing phenomena at the glass pane edges should be properly monitored and prevented, in order to maximize the benefits of the same pre-stressed rods. At the same time, it is also clear that the optimal configuration for pre-stressed GFRP rods should account for a combination of multiple aspects, including the glass-to-GFRP ratio, the R_{p0} amount of pre-stress, compared to the fracture stress of rods, as well as the basic mechanical properties of glass panes.

4.2.2. Parametric study and discussion

Aiming to explore the feasibility and potential of GFRP-embedded reinforcing rods, including pre-stressing forces of various magnitudes, Table 4 summarizes the major outcomes of the parametric FE study, highlighting for each model the load-deflection configurations associated to first cracking and collapse. Based also on Section 4.1, for clarity of presentation, the MR-n7 configuration was omitted from Table 4 (i.e. being intermediate to MR-n5 and MR-n10, with almost identical bending performance), giving evidence to initial force level

effects on the other embedded models only. In Fig. 10, to this aim, further non-dimensional comparisons are proposed, being representative of the post-cracked performance of the examined beams, while Fig. 11 presents additional comparative plots, as numerically derived in the form of load at the support – mid-span deflection curves.

Globally, important effects were generally noticed for the examined configurations, by imposing a certain value of pre-stress in rods.

In Table 4, pre-stressing effects are emphasized – given a beam geometry and a R_{p0} level, in the form of maximum uplift u_{0+} , as well as compressive $\sigma_{c,0}$ and tensile $\sigma_{t,0}$ stresses in glass due to P_0 only (i.e. Fig. 8). As a general rule, in this regard, a mostly linear proportionality was observed between the R_{p0} values and the corresponding stress effects in glass panes, at the end of Phase II. As a result, a proportional increase of elastic performances and first cracking configuration (i.e. F_1 and u_1 in Table 4) was generally noticed for all the beam configurations, as a function of the imposed pre-stressing value P_0 .

Worth of interest, in this regard, is the pre-stressing configuration of the MR-n10 beam, where the presence of rather uniform distribution of GFRP rods on the total height of the LG section mostly vanishes the expected effects of the same reinforcement rods, as well as of additional pre-stressing loads. This effect can be noticed in Table 4 and Fig. 10(a) and (b), especially for null/low pre-stressing levels ($R_{p0} = 0$ and 0.25), where coinciding R_F and R_u values were obtained for MR-n5

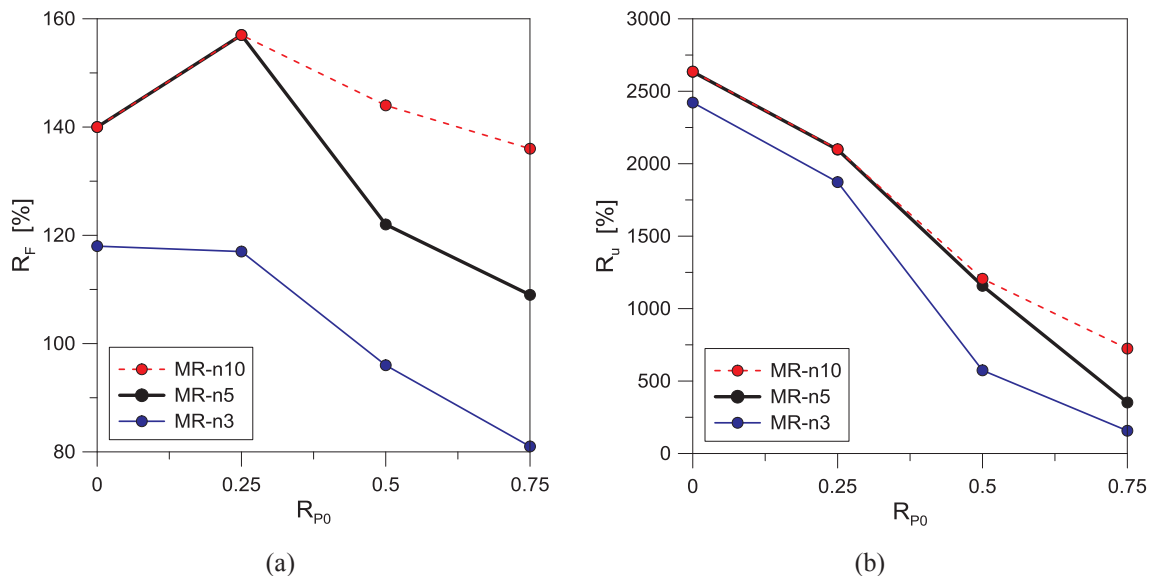


Fig. 10. Effects of pre-stressing forces on the post-cracked performance of examined beams, as numerically obtained in terms of (a) resistance and (b) deflection non-dimensional ratios (ABAQUS [19]).

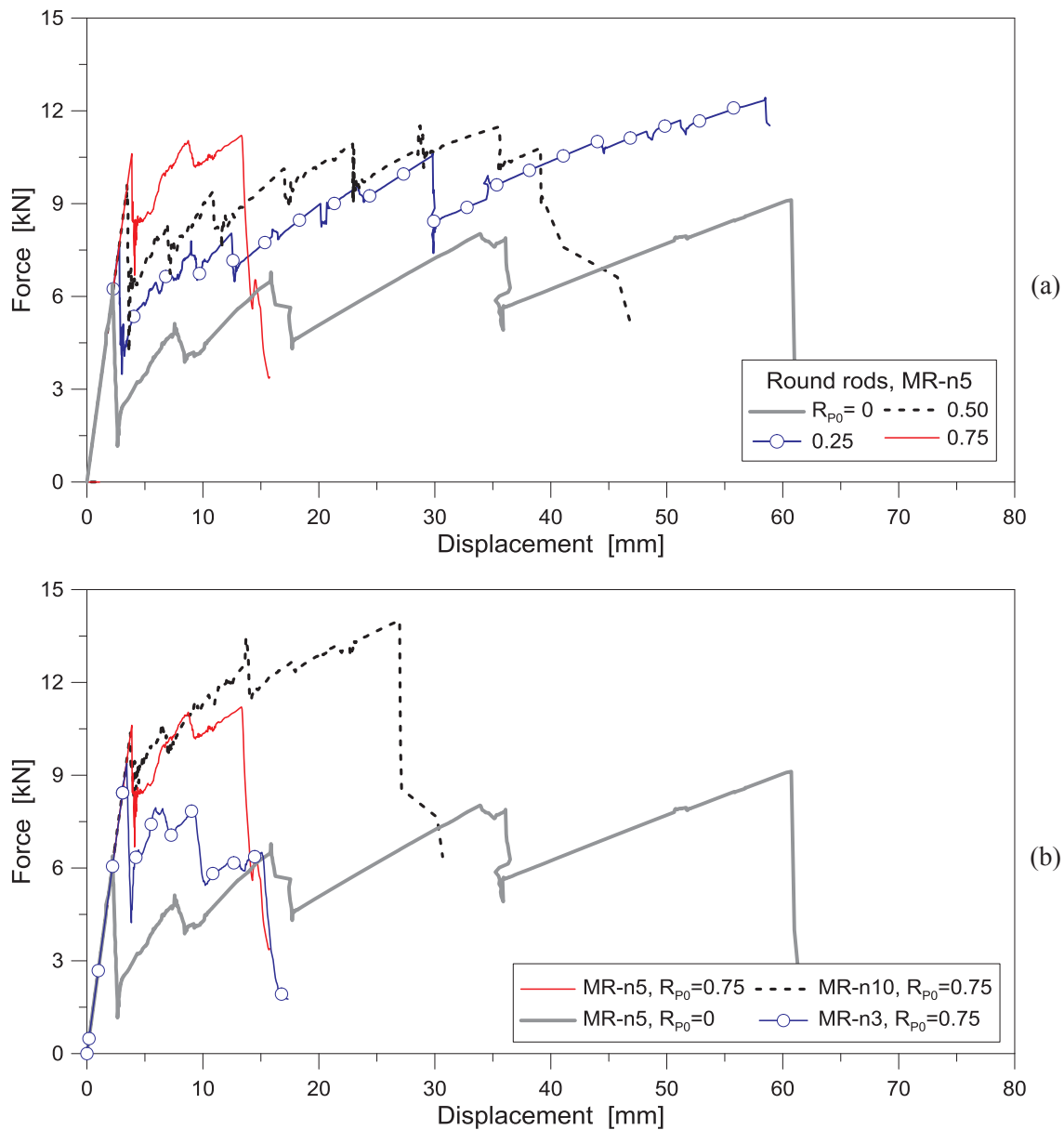


Fig. 11. Numerical (ABAQUS) load-displacement response of beam specimens with different amount of GFRP rods and initial pre-stress, in accordance with Table 4. (a) MR-n5 configuration, by changing R_{p0} and (b) comparison of various rod geometries, with $R_{p0} = 0.75$.

and MR-n10 beams.

As also in accordance with this latter observation, different effects were in fact observed for the same selected beams in the post-cracked stage, see Table 4 and Figs. 10 or 11.

In Fig. 11(a), for example, the MR-n5 beam response is shown by changing the amount of P_0 , i.e. by assuming a R_{p0} ratio equal respectively to 0, 0.25, 0.50 and 0.75. Basically, by increasing the R_{p0} value, the enhanced bending performance of beam specimens up to first cracking configuration is associated to opposite effects for the post-cracked stage. As a consequence of the same R_{p0} value, the GFRP rods are in fact lead to premature failure and their overall benefit for the laminated glass section vanishes. The latter aspect is also further emphasized in Table 4 in the form of R_f and R_u values, with decreasing values for higher R_{p0} levels. Given the MR-n5 configurations compared in Fig. 11(a), in this sense, the optimal R_{p0} value for the examined geometry was found to lie in the range of 0.25–0.50.

As far as the amount and distribution of GFRP rods modifies, see MR-n5 and MR-n10 plots in Fig. 11(b), the presence of initial pre-stressing forces ($R_{p0} = 0.75$, for selected curves) can be still associated

to minimum variations in the overall bending performance of the examined beams. In the case of the MR-n10 beam with increased number of rods, in addition, higher ductility was noticed compared to the MR-n5 system. This latter aspect can be justified by the activation of additional rods in the post-cracked stage only (i.e. enhanced residual resistance for cracked glass panes, as far as the top GFRP rods do not fail in tension), as well as due to the almost uniform initial compressive state for the glass panes as an effect of P_0 (see initial stress values in Table 4).

At the same time, in Fig. 11(b) it's possible to observe that decreasing the number of rods (i.e. MR-n3 curve) and imposing the same level of pre-stressing load P_0 would have mostly negative effects on the actual performance of the beam. While the first cracking configuration is in fact comparable to the MR-n5 one, this is not the case of post-cracked behaviour, being the MR-n3 beam performance typically associated to limited ultimate deflections, reduced post-cracked stiffness and an overall premature collapse.

5. Conclusions

In this paper, the feasibility and potential of a novel concept, consisting in structural glass beams reinforced with GFRP-embedded rods, has been investigated by means of computationally efficient Finite Element numerical models.

Taking advantage of past experimental studies, as well as on earlier numerical modelling assumptions and outcomes, the actual bending performance of different geometrical configurations has been explored, including variations in number, size and position of GFRP rods. In addition, possible benefits due to initial-pre-stressing forces imposed in the same rods have been also investigated.

As shown, rather stable and well promising behaviour was generally observed for the studied beams, even in presence of GFRP reinforcing tendons with limited size only, compared to the traditional laminated glass section. Major benefits were found to be emphasized especially in the post-cracked stage, where the embedded GFRP rods can provide residual stiffness and resistance, hence marked increase of ductility and redundancy, to mostly damaged glass components.

At the same time, the FE simulations partly summarized and discussed in the paper, proved the marked benefits deriving from additional pre-stressing forces for the same rods. Also in the latter case, however, the level of pre-stressing loads should be properly assessed, in order to avoid the occurrence of local damage phenomena in the beams components as well as to result in premature and fragile collapse for the same beams. In order to maximize the benefits of such concept towards the full development of safe design solutions and recommendations, in conclusion, a multitude of geometrical and mechanical aspects should be properly taking into account. It is expected, in this context, that discussed parametric investigations could provide useful background for the refinement of the explored design concept.

At the same time, it is also expected to further extend the actual study by assessing other intrinsic aspects, such as possible lateral-torsional buckling phenomena of the same beams, as well as their performance under extreme loads.

References

- [1] Palumbo M, Palumbo D, Mazzucchelli M. A new roof for the XIIIth century “Loggia de Vicari” (Arquà Petrarca – PD – Italy) based on structural glass trusses: a case study. *Proc Glass Process Days 2005*;2005:1–3.
- [2] Correia JR, Valarinho L, Branco FA. Post-cracking strength and ductility of glass-GFRP composite beams. *Compos Struct* 2011;93:2299–309.
- [3] Valarinho L, Correia JR, Branco FA. Experimental study on the flexural behaviour of multi-span transparent glass-GFRP composite beams. *Constr Build Mater* 2013;49:1041–53.
- [4] Speranzini E, Agnelli S. Flexural performance of hybrid beams made of glass and pultruded GFRP. *Constr Build Mater* 2015;94:249–62.
- [5] Olgaard AB, Nielsen JH. Design of mechanically reinforced glass beams: modelling and experiments. *Struct Eng Int* 2009;2(2009):130–6.
- [6] Bedon C, Louter C. Exploratory numerical analysis of SG-laminated reinforced glass beam experiments. *Eng Struct* 2014;75:457–68.
- [7] Martens K, Caspeele R, Belis J. Numerical investigation of two-sided reinforced laminated glass beams in statically indeterminate systems. *Glass Struct Eng* 2016;1(1):417–31.
- [8] Kreher K, Natterer J, Natterer J. Timber–glass composite girders for a hotel in Switzerland. *Struct Eng Int* 2004;2:149–51.
- [9] Blyberg L, Lang M, Lundstedt K, Schander M, Serrano E, Silfverhielm M, et al. Glass, timber and adhesive joints – innovative load bearing building components. *Constr Build Mater* 2014;55:470–8.
- [10] Martens K, Caspeele R, Belis J. Development of reinforced and post-tensioned glass beams: review of experimental research. *J Struct Eng* 2015;142(5):04015173.
- [11] Jordão S, Pinho M, Martins JP, Santiago A, Neves LC. Behaviour of laminated glass beams reinforced with pre-stressed cables. *Steel Constr* 2014;7:204–7. <http://dx.doi.org/10.1002/stco.201410027>.
- [12] Louter C, Cupać J, Lebet JP. Exploratory experimental investigations on post-tensioned structural glass beams. *J Façade Des Eng* 2014;2:3–18.
- [13] Engelmann M, Weller B. Post-tensioned glass beams for a 9 m span glass bridge. *Struct Eng Int* 2016;26:103–13. <http://dx.doi.org/10.2749/101686616X14555428759000>.
- [14] Cupać J, Martens K, Nussbaumer A, Belis J, Louter C. Experimental investigation of multi-span post-tensioned glass beams. *Glass Struct Eng* 2017;2(1):3–15.
- [15] Bedon C, Louter C. Finite-Element analysis of post-tensioned SG-laminated glass beams with mechanically anchored tendons. *Glass Struct Eng* 2016;1(1):19–37. <http://dx.doi.org/10.1007/s40940-0167>.
- [16] Bedon C, Louter C. Finite Element analysis of post-tensioned SG-laminated glass beams with adhesively bonded steel tendons. *Compos Struct* 2017;167:238–50.
- [17] Bedon C, Louter C. Numerical analysis of glass-FRP post-tensioned beams – review and assessment. *Compos Struct* 2017. <http://dx.doi.org/10.1016/j.compstruct.2017.06.060>. published online.
- [18] Louter C, Leung C, Kolstein H, Vamborský J. Structural glass beams with embedded Glass Fibre Reinforcement. In: *Proceedings of challenging glass 2 – conference on architectural and structural applications of glass*, TU Delft, May 2010, 2010.
- [19] Simulia. ABAQUS v. 6.14 computer software and online documentation, Dassault Systems, Providence, RI, USA, 2016.
- [20] SentryGlas® Ionoplast Interlayer – Technical Data Sheet, www.sentryglas.com (accessed September 2017).
- [21] R & G, Chapter 08. Glass, aramid and carbon fibre, R & G composite handbook edition 8, www.r-g.de.
- [22] TOHO TENAX EUROPE GmbH, Datasheet Tenax HT5131, www.tohotenax-eu.com.
- [23] EN 572–2:2004. Glass in buildings-Basic soda lime silicate glass products. CEN, Brussels, Belgium.
- [24] CNR-DT 210/2013. Istruzioni per la progettazione, l’esecuzione ed il controllo di costruzioni con elementi strutturali in vetro [Technical Document, in Italian], National Research Council, Rome, Italy (2013).
- [25] D Callewaert (2011). Stiffness of Glass/Ionomer Laminates in Structural Applications. Ph.D. Dissertation, Ghent University.
- [26] Santarsiero M, Louter C, Nussbaumer A. The mechanical behaviour of SentryGlas® ionomer and TSSA silicon bulk materials at different temperatures and strain rates under uniaxial tensile stress state. *Glass Struct Eng* 2016. <http://dx.doi.org/10.1007/s40940-016-0018-1>.
- [27] Haldimann M, Luible A, Overend M. Structural use of glass. IABSE, ISBN 978-3-85748-119-2, 2008.
- [28] Bedon C, Amadio C. Design buckling curves for glass columns and beams. *Struct Build* 2015;168(7):514–26.
- [29] Luible A, Schärer D. Lateral torsional buckling of glass beams with continuous lateral supports. *Glass Struct Eng* 2016;1(1):153–71.
- [30] Sonck D, Belis J. Elastic lateral-torsional buckling of glass beams with continuous lateral restraints. *Glass Struct Eng* 2016;1(1):173–94.
- [31] Bedon C, Belis J, Amadio C. Structural assessment and lateral-torsional buckling design of glass beams restrained by continuous sealant joints. *Eng Struct* 2015;11:214–9.